The spontaneous passivation of multi principal element alloys II: The effect of Mn in the CoCrFeNiMn family

Chenyang Xie, Junsoo Han, Fan Sun, Kevin Ogle

▶ **To cite this version:**

Chenyang Xie, Junsoo Han, Fan Sun, Kevin Ogle. The spontaneous passivation of multi principal element alloys II: The effect of Mn in the CoCrFeNiMn family. Corrosion Science, 2025, 244, pp.112642. ⟨10.1016/j.corsci.2024.112642⟩. ⟨hal-04844800⟩

HAL Id: hal-04844800

https://hal.sorbonne-universite.fr/hal-04844800v1

Submitted on 18 Dec 2024

HAL is a multi-disciplinary open access archive for the deposit and dissemination of scientific research documents, whether they are published or not. The documents may come from teaching and research institutions in France or abroad, or from public or private research centers.

L'archive ouverte pluridisciplinaire **HAL**, est destinée au dépôt et à la diffusion de documents scientifiques de niveau recherche, publiés ou non, émanant des établissements d'enseignement et de recherche français ou étrangers, des laboratoires publics ou privés.

HAL Authorization

Journal Pre-proof

The spontaneous passivation of multi principal element alloys II: The effect of Mn in the CoCrFeNiMn family

Chenyang Xie, Junsoo Han, Fan Sun, Kevin Ogle

PII: S0010-938X(24)00839-4

DOI: https://doi.org/10.1016/j.corsci.2024.112642

Reference: CS112642

To appear in: *Corrosion Science*

Received date: 8 November 2024
Revised date: 9 December 2024
Accepted date: 13 December 2024

Please cite this article as: Chenyang Xie, Junsoo Han, Fan Sun and Kevin Ogle, The spontaneous passivation of multi principal element alloys II: The effect of Mn in the CoCrFeNiMn family, *Corrosion Science,* (2024) doi:https://doi.org/10.1016/j.corsci.2024.112642

This is a PDF file of an article that has undergone enhancements after acceptance, such as the addition of a cover page and metadata, and formatting for readability, but it is not yet the definitive version of record. This version will undergo additional copyediting, typesetting and review before it is published in its final form, but we are providing this version to give early visibility of the article. Please note that, during the production process, errors may be discovered which could affect the content, and all legal disclaimers that apply to the journal pertain.

© 2024 Published by Elsevier Ltd.

The spontaneous passivation of multi principal element alloys II: The effect of Mn in the CoCrFeNiMn family

Chenyang Xie[1], Junsoo Han[2], Fan Sun[1], Kevin Ogle[1]

[1] Chimie ParisTech, PSL University, CNRS, Institut de Recherche Chimie Paris (IRCP), F-75005 Paris, France

[2] Sorbonne Université, CNRS, Laboratoire Interfaces et Systèmes Electrochimiques (LISE), F-75005 Paris, France

Abstract:

The influence of at% Mn on the polarization and spontaneous passivation of $(CoCrFeNi)_{100-x}Mn_x$ (at%) alloys in aerated 0.1 M H_2SO_4 was investigated using atomic emission spectroelectrochemistry. At 0 – 6.5 at% Mn, spontaneous passivation occurred but at ≥ 10 at% Mn, the beneficial effect of Cr was completely negated. Spontaneous passivation could be predicted from Evans diagrams in which total current was decoupled into anodic dissolution and the cathodic components. Passivation occurred in two stages: rapid reaction with significant Cr enrichment; slower reaction with less enrichments. Differences between spontaneous and potentiodynamic passivation are discussed and interpreted with rate vs. free potential curves.

Keywords: Multi-principal element alloys (MPEA); Spontaneous passivation; Active-passive transition, Mn, AESEC

Journal Pre-proof

1. Introduction

Understanding the contribution of the individual components of an alloy to its overall corrosion resistance is a key factor in optimizing alloy composition. While this is true for all alloys, it is particularly critical for multi-principal element alloys (MPEAs) where the vast compositional space renders the conventional trial and error method more difficult [1,2]. The classic example of an MPEA is the high-entropy Cantor alloy (equimolar Co-Cr-Fe-Mn-Ni) [3,4]. Cr and Mn are the two elements which have the most marked effect on the corrosion resistance of the Cantor alloy. Cr is of course, the main element to promote corrosion resistance. For example, Aiso *et al.* [5] demonstrated that the quaternary Co-Fe-Mn-Ni alloy with 0% Cr, showed only a very limited passive domain in 0.1 M H_2SO_4 and no passivation in 0.1 M NaCl.

The negative effect of Mn on passivation

As for most alloys containing Cr above a threshold value (for example, 12 to 13 wt% for Fe-Cr alloys [6,7,8]), it has been well documented that Cr is the primary element contributing to the formation of the passive film [9,10]. By contrast Mn has been demonstrated to considerably lower the corrosion resistance of the Cantor alloy. Citing again Aiso *et al.* [5], they demonstrated that the removal of Mn lowered the critical current of the CoCrFeNi alloy by an order of magnitude in H_2SO_4, without significantly changing either the passive current or transpassive potential. Similar results were obtained by Yang *et al.* [11] by comparing CoFeNiCr with various additions of Mn. These results suggest that the effect of Mn was primarily on the kinetics of passivation rather than the nature of the film itself. This model was developed in detail by [11]*et al.* based on modeling of electrochemical impedance spectra suggesting that Mn significantly degrades the general corrosion resistance of the CoFeNiMnCr alloy in 0.1 M H_2SO_4 by suppressing the passivation process. Likewise, in NaCl, the removal of Mn from the Cantor alloy (CoCrFeNi) raised the pitting potential by nearly 1 V demonstrating that pit repassivation was hindered by the presence of Mn [5]. D.

Journal Pre-proof

Dworschak *et al.* [12] proposed that Mn catalyzes the dissolution of Fe and Cr, preventing the formation of a stable passive film in a 1 mM NaCl based on their investigation of equiatomic alloys ranging from binary to quinary compositions within the Cantor family.

It is beyond the scope of this work to give a complete review of the literature however, the negative effect of Mn in the Cantor alloy has been well documented in other publications including sulfuric acid [13,14] and chloride [15,16,17,18] as well as for the related, $Al_{0.3}Cr_{0.5}Fe_2Mn_xMo_{0.15}Ni_{1.5}Ti_{0.3}$ [19] in chloride. For stainless steel in chloride solution, Mn has often been associated with the formation of sulfide precipitates which serve as nucleation sites for pitting corrosion sulfide [20,21,22,23,24,25]. However, Park and Kwon [26] used capillary electrochemical methods to isolate the pure phase of an Fe-18Cr alloy, and in this way, demonstrated that dissolved Mn in the inclusion free matrix increased the critical current and decreased the pitting potential in 0.1 M HCl solution. They also demonstrated that Mn slowed the kinetics of repassivation following a scratch in 0.1 M NaCl.

Given its high reactivity, it is not surprising that the addition of Mn to a passivating alloy would diminish the efficiency of passive film formation. The equilibrium potential - pH (Pourbaix) diagram indicates that in acidic solution, the stable species is Mn^{2+} (aq), over the entire range of water stability [27,28] with MnO_2 forming only at the extreme upper limit, coincident with oxygen formation.

$$Mn \rightarrow Mn^{2+} + 2\ e^- \qquad E° = -1.179\ V\ vs.\ SHE$$

$$Mn^{2+} + 2H_2O \rightarrow MnO_2 + 4H_2O + 2e^- \qquad E° = 1.228\ V\ vs.\ SHE$$

The passivation of Mn in acid solution is only possible under very special conditions such as in the presence of phosphoric acid [29].

Although the previously cited works concluded that the addition of Mn did not affect the barrier properties of the passive film formed by potentiostatic means, much of the available literature has focused on the structure and composition of the passive film. For example, Luo *et al.* [13] attributed the lower corrosion resistance of the

Journal Pre-proof

Cantor alloy in sulfuric acid to the enrichment of Fe and Mn at the expense of Cr in the passive film. Wang *et al.* [10] demonstrated by X-ray photoelectron spectroscopy (XPS) that the oxide film on the equiatomic CoCrFeMnNi alloy in 0.05 M H_2SO_4, after either anodic applied potential or open circuit conditions, consisted of an inner Cr- and Mn-based layer and an outer layer consisting of a Cr/Fe/Co mixture. Han *et al.* [16] demonstrated that an enrichment in Mn(II) species relative to Cr(III) in the oxide was identified by XPS for a $Ni_{38}Fe_{20}Cr_{22}Mn_{10}Co_{10}$ after polarization in the passive domain (0.1 V_{SCE}) in a 0.1 M NaCl electrolyte at pH=4.

Spontaneous Passivation

Corrosion studies of MPEAs are mainly based on conventional electrochemical parameters such as passive current, pitting potential, etc. A database of relevant information has been compiled by Nyby *et al.* [30]. In practice however, the ability of an alloy to spontaneously repassivate after damage to the passive film by abrasion or by aggressive attack as in pitting is often the factor that determines the ultimate corrosion resistance in the field. Spontaneous passivation at the free, or open circuit potential (OCP), implies that both the cathodic and anodic reactions occur on the same surface. Therefore, the mechanisms and rates of the reactions may differ significantly from the situation where passivation is induced by the power supply of a potentiostat and the cathodic reaction occurs at a distant counter electrode.

In a previous article [31], (Part I of this series) we investigated the effect of a variable at% Cr on the spontaneous passivation of $(CoFeNi)_{100-x}Cr_x$ (at%) using the atomic emission spectroelectrochemistry (AESEC) technique by correlating the the spontaneous passivation kinetics with the active-passive transition and the critical dissolution rate obtained during potentiodynamic experiments. In this work, we use the same methodology to investigate the detrimental effect of variable at% Mn on the kinetics of spontaneous passivation for a series of $(CoCrFeNi)_{100-x}Mn_x$ (at%) MPEAs in 0.1 M H_2SO_4.

Journal Pre-proof

2. Method and Materials

A series of $(CoCrFeNi)_{(100-x)}Mn_x$ ($0 \leq x \leq 20$ at%) alloys was prepared by adding variable quantities of Mn (99.95%) to an equiatomic CoCrFeNi master alloy. The alloys are denoted based on at% of Mn, for example, 6.5 at% Mn as $Mn_{6.5}$. The metallurgical characterization and composition of the of $(CoCrFeNi)_{100-x}Mn_x$ alloys are summarized in **Table 1** with a detailed description in the following section. The master alloy was prepared from high-purity metals Co, Cr, Fe, Ni (99.95%, Goodfellow Inc.), remelted five times and cast to a bar ingot (150 x 15 x 15 mm^3) by suction casting in a Buhler AM500 arc melting furnace. The master alloy in the form of a bar was subsequently divided into small pieces of 15 - 20 g. Corresponding alloy components were formulated by adding the respective amounts of Mn (99.95%) and subjected to three melting cycles to button ingots. After removing the surface oxides by grinding, the button ingots were cold rolled with a reduction rate of ~75 % to 0.5 mm thickness sheets. The sheets were then annealed in vacuum tubular furnace under 2.0×10^{-5} Pa at 1273 K with subsequent water quenching for recrystallization and homogenization. The samples were cut to square pieces of ~15 mm × 25 mm in size, grinding with P600 and P1200 SiC paper in sequence and cleaned in ultrasonic bath with acetone and dried with flowing N_2 gas.

Metallurgic characterization

X-ray diffraction (XRD) analysis was performed on a PANalytical X'Pert diffractometer, scanning from 20° to 100° (2θ) with Cu K_α radiation at 45 kV and 40 mA. Quantitative energy dispersive X-ray spectroscopy (EDX) analysis was conducted with a Zeiss Supra35 field emission gun scanning electron microscopy (FEG-SEM) at 15 kV, equipped with a Bruker XFLASH 6/60 system. The as-quenched samples for electron backscatter diffraction (EBSD) were electropolished to a mirror-like finish with 4% perchloric acid in methanol at 0 °C. EBSD mapping used a Zeiss Merlin FEG-SEM at 20

Journal Pre-proof

kV and a Bruker EBSD camera. Inverse pole figures (IPF) and grain size were analyzed with OIM™ software, using the equivalent circular diameter (ECD) method.

Table 1 Nominal and EDX measured composition, alongside the phase information and grain sizes determined through EBSD image analysis. Grain size measurements adhere to the equivalent circular diameter (ECD) method. All alloys show a single FCC phase and a slight increase in grain size with the incremental addition of Mn. The EDX-derived composition closely aligns with the nominal composition (within ±1 at%).

Alloy	Method	Co	Cr	Fe	Ni	Mn	Phase	Grain size / µm (±1 µm)
Mn_0	*Nominal*	***25.0***	***25.0***	***25.0***	***25.0***	***0.0***	FCC	6.2
	EDX	25.6	24.6	25.0	24.8	-		
$Mn_{1.5}$	*Nominal*	***24.6***	***24.6***	***24.6***	***24.6***	***1.5***	FCC	7.9
	EDX	24.8	24.7	24.7	24.2	1.5		
Mn_5	*Nominal*	***23.8***	***23.8***	***23.8***	***23.8***	***5.0***	FCC	6.3
	EDX	23.2	23.8	23.6	24.3	5.2		
$Mn_{6.5}$	*Nominal*	***23.4***	***23.4***	***23.4***	***23.4***	***6.5***	FCC	6.9
	EDX	23.1	23.4	23.4	23.3	6.9		
Mn_{10}	*Nominal*	***22.5***	***22.5***	***22.5***	***22.5***	***10.0***	FCC	9.2
	EDX	21.9	22.5	22.3	23.2	10.2		
Mn_{20}	*Nominal*	***20.0***	***20.0***	***20.0***	***20.0***	***20.0***	FCC	11.4
	EDX	19.5	20.3	20.1	20.3	19.9		

Electrochemical Experiments

The AESEC technique and the details of the experimental protocols used in this work have been described in Part I of this work [31]. The principles on AESEC have been published elsewhere [32]. The AESEC technique operates by utilizing a flow cell connected to an inductively coupled plasma – atomic emission spectrometer (ICP-AES), enabling on-line quantitative analysis of elements dissolved in the electrolyte. An Ultima 2C® (Horiba France) ICP-AES was used for the AESEC analysis. A Gamry Reference 600® potentiostat was used to perform electrochemical experiments. A Pt

Journal Pre-proof

counter electrode and a saturated calomel electrode (SCE) reference electrode were used.

A 0.1 M H_2SO_4 electrolyte was used in all experiments, prepared using reagent grade 95% H_2SO_4 and ultrapure water (Millipore, 18.2 MΩ cm at 25°C). The electrolytes were naturally aerated by bubbling air into the solution with an air pump, 30 mins before and during the experiments. All experiments were conducted using a specially designed AESEC flow cell with a flow rate *f* of 2.7 ml min^{-1}. The ICP-AES spectral lines used in this work and their detection limits for the conditions of the study are given in **Table 2**.

For potentiodynamic polarization measurements, an initial activation step was performed by applying −0.7 V_{SCE} for five minutes, followed by a potential scan from −0.7 V_{SCE} to 1.1 V_{SCE} at 0.5 mV s^{-1}. The potential was corrected afterwards for the uncompenstated electrolyte resistance, R_Ω = 55 Ω, as determined by high frequency electrochemical impedance spectroscopy (EIS). Spontaneous passivation measurements were conducted in three identical cycles, with each cycle proceeding as follows: −0.7 V_{SCE} for 10 min (activating the surface), open circuit measurement for 30 mins (spontaneous passivation/dissolution), and −0.7 V_{SCE} for 10 min (surface reactivation).

ICP-AES intensity signals were converted into elemental concentration (C_M, M = element) using standard calibration methodology. The elemental dissolution rates (v_M) were calculated from the downstream concentration as follows:

$$v_M = f\, C_M / A \quad (1.)$$

where *f* is the flow rate of the electrochemical flow cell, and A is the exposed surface area of the sample. The total dissolution rate (v_{diss}) of all elements can be written as:

$$v_{diss} = \sum_M v_M \quad (2.)$$

which may be converted into the equivalent dissolution current density (j_{diss}) to facilitate comparison with the electrical (j_e) current as:

$$j_{diss} = F \sum_M n_M v_M \quad (3.)$$

Journal Pre-proof

where n_M is the number of electrons exchanged for the dissolution of M, and F is the Faraday constant. In this work, the estimated the dissolved valence states were n_M = 2 for Fe, Ni, Co and Mn, and n=3 for Cr in the potential range from -0.6 V_{SCE} to 0.1 V_{SCE} in agreement with published thermodynamic calculation for pure elements [27] and for alloys using the CALPHAD approach [33]. Additional data treatment parameters such as cumulative dissolution quantities (Q_{diss}), or the estimated surface enrichment of element M, (Θ_M) and its derivative ($\dot{\Theta}_M$), were calculated using formulas outlined in ref. [31].

Table 2 Detection limits for Co, Cr, Fe, Mn and Ni in 0.1 M H_2SO_4 at 25 °C with a flowrate of f = 2.7 ml min^{-1}. Detection limits are defined as three times the standard deviation of the background signal of the electrolyte at the given wavelength. Detection limits are either expressed as concentration ($C_{3\sigma}$) or as equivalent dissolution rates (ν_{diss}(eq)) calculated from Eq. 1. Error bars represent the standard deviation over 12 repeated experiments.

Element	Wavelength (nm)	$C_{3\sigma}$ (ppb)	ν_{diss}(eq) (pmol s^{-1})
Co	228.62	5.4 ± 0.5	4.1 ± 0.4
Cr	267.72	4.2 ± 0.4	3.6 ± 0.4
Fe	259.94	3.1 ± 0.7	2.5 ± 0.6
Mn	257.61	0.46 ± 0.04	0.37 ± 0.03
Ni	231.60	10.2 ± 1.6	8.0 ± 1.1

3. Results

3.1 Metallurgy characterization

Table 1 compares the nominal composition with that measured by EDX for all alloys. Also shown is the phase information and grain sizes determined through EBSD image analysis. The EDX-derived composition closely aligned with the nominal composition (± 1 at%). The surface showed an absence of discernible inclusions, precipitates, or defects. All alloys exhibited a single face-centered cubic (FCC) structure, as indicated by the EBSD inverse pole figures (IPF) and XRD spectra in **Fig. 1**.

Journal Pre-proof

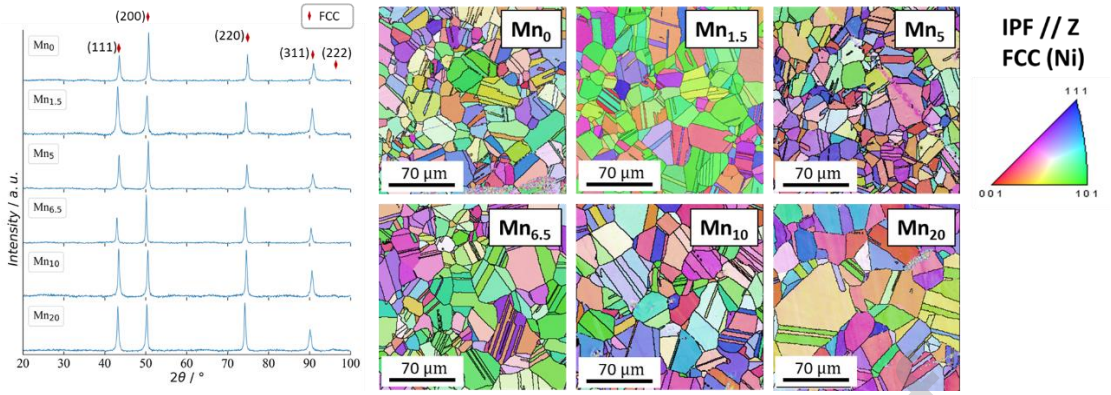

Fig. 1. Left: XRD spectra for all $(CoCrFeNi)_{100-x}Mn_x$ alloys (at%) scan from 20° to 100° (2θ) with Cu K_α radiation operating at 45 kV and 40 mA. The spectra confirm the single face-centered cubic (FCC) crystal structure for all alloys. **Right:** Inverse pole figure (IPF) maps of $(CoCrFeNi)_{100-x}Mn_x$ alloys (at%). These maps reveal a single FCC structure across all alloy compositions without a preferred grain orientation, indicating homogeneous microstructural characteristics. Grain size details are provided in **Table 1**. This uniformity in grain structure across the alloys suggests that Mn substitution does not significantly alter the crystallographic texture under the applied heat treatment conditions.

3.2 Element resolved polarization curves

A global vision of the electrochemistry of the alloys may be obtained from the conventional polarization curves (j_e – E_{ap} profile, j_e = electrochemical current density; E_{ap} = the applied potential) of **Fig. 2.** The i R_Ω drop was corrected based on the R_Ω = 55 Ω determined from high frequency EIS. The effect of R_Ω was only apparent in the cathodic domain where the current rises above 1 mA. The electrochemical parameters determined from these curves can be found in **Table 3**.

The cathodic, passive, and transpassive domains were essentially identical for all alloys with the main differences concentrated in the active-passive transition potential range in agreement with previous work (Aiso *et al.* [5]). The Mn_{20} alloy revealed a j_{crit} more than an order of magnitude larger that of the alloys of lower Mn content (see **Table 3**). Likewise, the zero current potential ($E_{j=0}$) values for Mn_{20} were shifted by nearly 75 mV in the cathodic direction as compared to the alloys of lower Mn content. By contrast, the potentials of the active-passive transitions (j_{crit},E_{pp}) were nearly identical for all alloys, at −0.284 to −0.236 V_{SCE}.

Journal Pre-proof

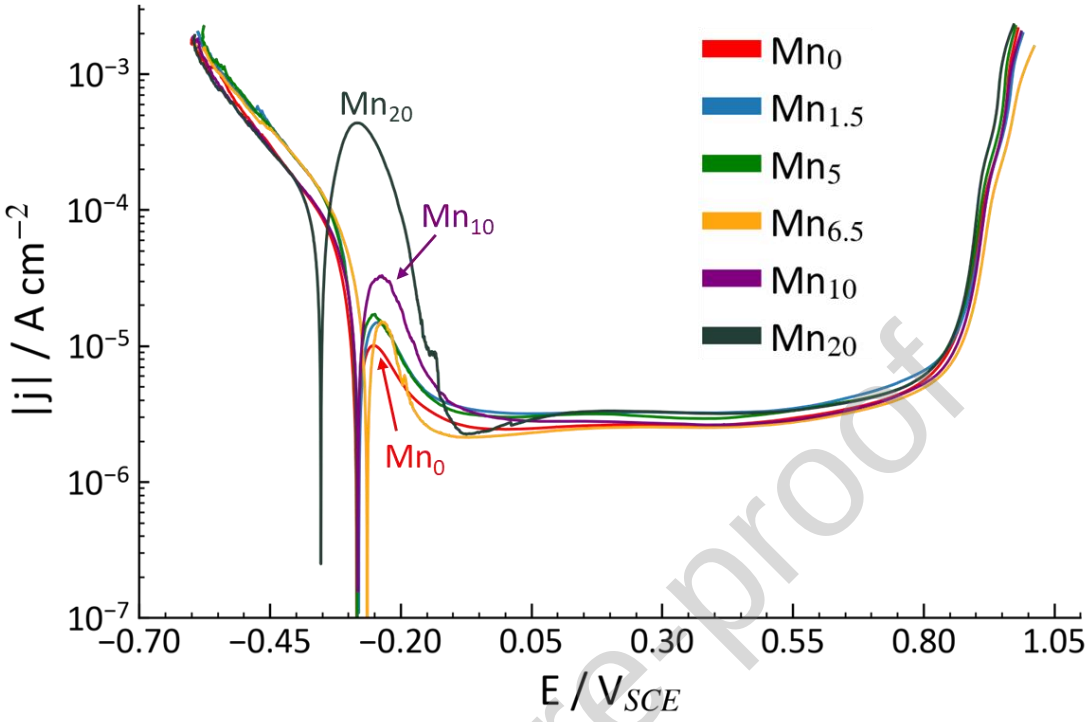

Fig. 2. The polarization curves of $(CoCrFeNi)_{100-x}Mn_x$ alloys (at%) in 0.1 M H_2SO_4 (air saturated, ambient temperature) from −0.7 to 1.1 V_{SCE} with a scan rate of 0.5 mV s^{-1} and a flow rate of 2.7 ml min^{-1}. The iR_Ω drop was corrected based on R_Ω = 55 Ω. Electrochemical parameters derived from these curves may be found in **Table 3**.

Table 3 Electrochemical parameters obtained from polarization curves in **Fig. 2** and equivalent critical current densities obtained from the AESEC measurements. $E_{pp,diss}$ is the potential where elemental dissolution rates reach a maximum value in active-passive transition domain, and $j_{crit,diss}$ is the equivalent current.

Alloys	$E_{j=0}$ / V_{SCE}	E_{pp} / V_{SCE}	E_{pp} - iR_Ω/ V_{SCE}	$E_{pp,diss}$ / V_{SCE}	$E_{pp,diss}$-iR_Ω / V_{SCE}	j_{crit} / µA cm^{-2}	$j_{crit,diss}$ / µA cm^{-2}
Mn_0	−0.283	−0.250	−0.250	*−0.316*	*−0.314*	10.1	*9.7*
$Mn_{1.5}$	−0.280	−0.242	−0.242	*−0.347*	*−0.341*	14.9	*24.2*
Mn_5	−0.282	−0.248	−0.248	*−0.271*	*−0.272*	17.1	*29.6*
$Mn_{6.5}$	−0.263	−0.235	−0.236	*−0.235*	*−0.236*	15.1	*22.7*
Mn_{10}	−0.281	−0.233	−0.235	*−0.204*	*−0.205*	32.9	*37.0*
Mn_{20}	−0.352	−0.261	−0.284	*−0.248*	*−0.271*	435.5	*480*

The conventional polarization curves of **Fig. 2** offer a broad view of the electrochemical activity of the material; however, the anodic behavior of the alloy may

be hidden by the cathodic reaction. Further insight into the anodic dissolution kinetics may be gained by consideration of the experimental Evans diagrams (EED) of **Fig. 3**. The EED presents both the total electrochemical current density, j_e from the potentiostat, and the total dissolution current density, j_{diss}. A dashed straight line is drawn representing the Tafel slope of the cathodic process extrapolated into the active to passive transition region. This may be used as a guide to predict spontaneous passivation. The driving force for the spontaneous passivation process is the cathodic reaction occurring on the active surface which must be sufficient to drive the anodic dissolution rate up to the critical value ($j_{crit,diss}$) [31,9]. This total cathodic activity may be estimated by the extrapolated Tafel line. Thus for spontaneous passivation to occur, the extrapolated cathodic activity (j_{cat}) must be greater than the critical dissolution current (j_{cat}) > $j_{diss,crit}$ at $E_{pp,diss}$.

In all cases, the onset of anodic dissolution was shifted below the $E_{j=0}$, under the cathodic current wave. For at% Mn = 0 and 1.5, the entire active to passive transition and $E_{pp,diss}$ were shifted below $E_{j=0}$ and were not detectable in the j_e vs E profile. The maximum difference between $E_{pp,diss}$ and E_{pp} reaches 0.099 V. And a single dissolution peak was observed with a maximum ($j_{crit,diss}$) of 9.7 and 27.2μA cm^{-2}, respectively. Two peaks were observed in the active to passive dissolution transient for Mn at% = 5, 6.5 and 10. The $E_{pp,diss}$ value shifted closer to that of the E_{pp}, with a maximum difference of 0.03 V. However, the $j_{crit,diss}$ is similar to that of $Mn_{1.5}$ alloy, ranging from 20 to 37.0 μA cm^{-2}. A critical concentration of Mn was apparent, somewhere between 6.5 at% and 20 at% where both j_{crit} and $j_{crit,diss}$ increased by more than an order of magnitude.

This abrupt increase in the critical current density reflects the lowered efficiency of passivation associated with increased at% Mn. Under these conditions, $j_{crit,diss}$ was nearly equivalent within experimental error to $j_{crit,}$, reflecting a nearly 100% faradaic yield of dissolution. Both $j_{crit,diss}$ and $j_{crit,}$ were significantly more intense than the extrapolated cathodic current suggesting that spontaneous passivation would not occur under the conditions of these experiments.

Journal Pre-proof

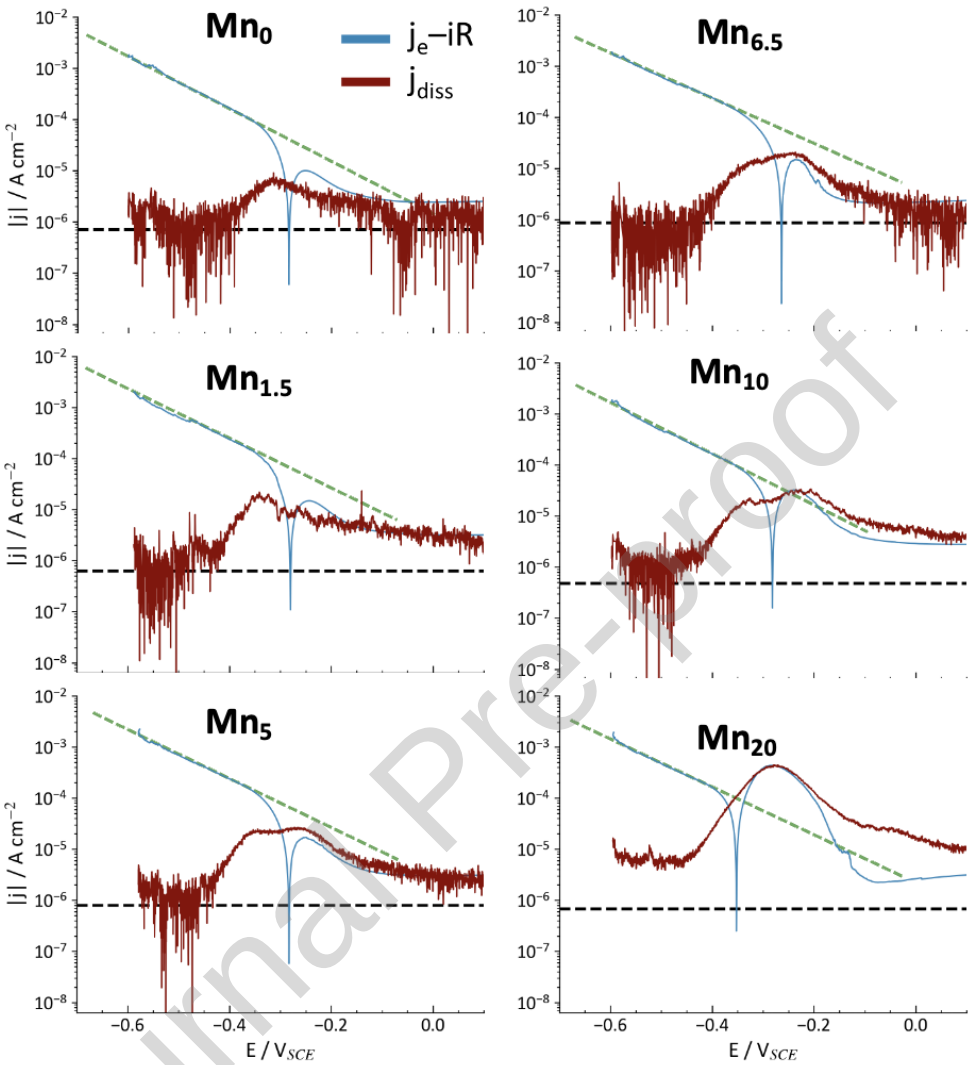

Fig. 3. The iR_Ω corrected polarization (j_e–iR_Ω, in blue) and dissolution equivalent (j_{diss}, in red-brown) current density curves for Mn_x alloys, where the Tafel slope of cathodic current is denoted by a green dashed line, and the detection limit is represented by a black horizontal dashed line. The uncorrected polarization curves are plotted as green dashed curves to show the influence of the iR_Ω correction which is insignificant in the active to passive transition except for Mn_{20}.

To further explore the dissolution behavior of each element during the active-passive transition process, the elemental dissolution curves of all alloys during polarization from −0.6 to 0.1 V_{SCE} are displayed in **Fig. 4**. The ν_{Mn} has been normalized to the nominal composition as indicated such that for congruent dissolution, all elements should have an identical dissolution rate.

A single dissolution transient was observed for 0 and 1.5 at% Mn. At higher Mn

concentration, two poorly resolved peaks were observed, labeled as a1 and a2 in **Fig. 4.** The dashed lines a1 and a2 shown for all curves, represent the potentials for the two anodic dissolution peaks visible in the Mn_5 alloy at −0.348 V_{SCE} and −0.262 V_{SCE}, respectively. The a2 peak appeared to grow as the at% Mn increased. For the Mn-free alloy, the active-passive transition peak fell between a1 and a2. With the addition of 1.5 at% Mn, this peak shifted to the a1 potential, accompanied by a minor peak near a2. As the Mn content reached 5 at%, both peaks became more pronounced, with dissolution at a1 lower than at a2. With 6.5 at% Mn, the peak at a2 was significantly higher than at a1, with a1 becoming less distinct. When reaching 20 at% Mn, only the peak at a2 was discernible. It is of interest to note that the addition of Mn to a Fe- 18Cr (wt%) in 0.1 M HCl, lead to the appearance of two poorly resolved anodic peaks in ref. [26].

The occurrence of two peaks in the dissolution transient suggests two distinct mechanisms of passivation. The stoichiometry of dissolution did not appear to change in a statistically significant manner between the a1 and a2 peak, although the high noise level of the data makes a precise measurement of the stoichiometry difficult. It may be observed in **Fig. 4**, that the Cr dissolution rate was always lower than the other elements suggesting the enrichment of Cr during the active to passive transition. The Mn_{20} showed a very high dissolution rate of Fe.

Journal Pre-proof

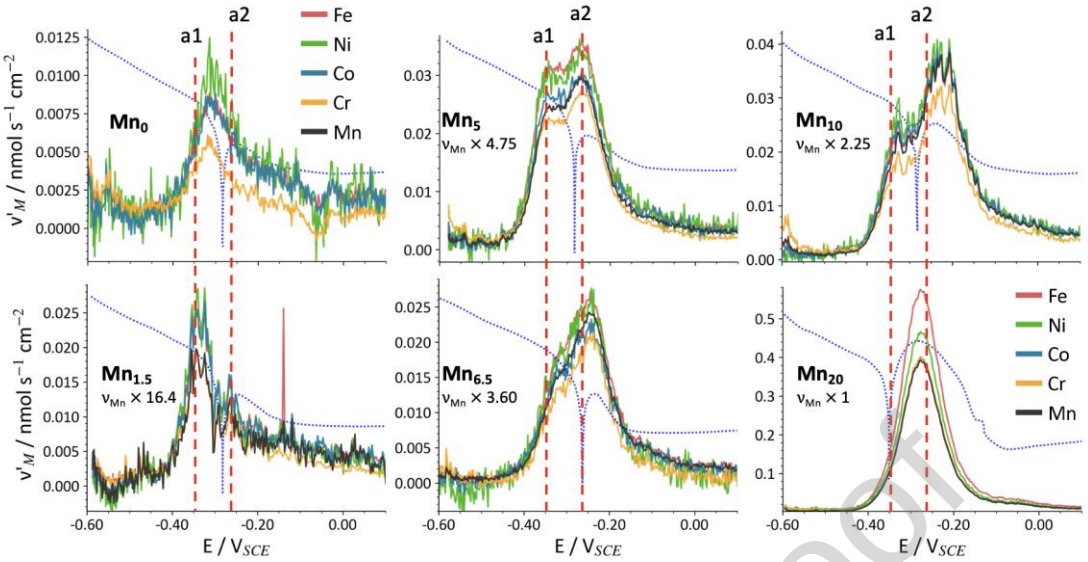

Fig. 4. The stoichiometric dissolution rates for $(CoCrFeNi)_{100-x}Mn_x$ alloys (at%) during the polarization (see **Fig. 2** and **3**), the iR drop is correct corrected based on the R_Ω = 55 Ω, Mn is normalized based on the nominal composition. The a1 and a2 dashed lines correspond to potentials of −0.35 V_{SCE} and −0.25 V_{SCE}, respectively. The form of the $j_e - E_{ap}$ profile (not to scale) from Fig. 3 is traced as a blue dashed curve in the background as a reference.

The results of this section demonstrate that the increase in at% Mn leads to a destabilization of the alloy reflected in the enhanced critical dissolution rate. A critical concentration of Mn was apparent, somewhere between 10 at% and 20 at%, where both j_{crit} and $j_{crit,diss}$ rose more than an order of magnitude, surpassing the extrapolated cathodic activity of the environment. At 5 at% Mn and above, anodic dissolution formed two discrete but poorly resolved transients.

3.3 Spontaneous passivation

The kinetics of spontaneous passivation were investigated using the experimental protocol previously developed [31]. The alloy was initially depassivated by applying a potentiostatic cathodic hold at -0.7 V vs. SCE. The system was then released to the open circuit potential (E_{OC}) and the elemental dissolution rates (ν_M) and the E_{OC} were monitored as a function of time. The kinetics of spontaneous passivation may be determined from the decrease in the dissolution rate. The enrichment of alloying elements on the surface of the material may be determined from the stoichiometry of dissolution.

Journal Pre-proof

Fig. 5 presents the dissolution rate (b) and E_{OC} (a) as a function of time for first cycle of the spontaneous passivation experiments for all alloys. The other cycles can be found in supplementary materials (**Fig. S1**). The Mn_{10} and Mn_{20} alloys did not undergo spontaneous passivation on the time scale of these experiments, and only a single experimental cycle was conducted due to the high dissolution rate, which altered the surface, rendering subsequent cycles ineffective. Rather, they approached a steady dissolution rate of approximately 0.6 nmol s^{-1} cm^{-2}. The dissolution rate of Mn_{20} was still rising at the end of the experiment. Both showed a relatively stable E_{OC} between −0.33 to −0.35 V_{SCE}.

These results are consistent with the predictions from the EED of **Fig. 3** as the $j_{crit,diss}$ lies above the extrapolated cathodic Tafel line. For the other alloys, spontaneous passivation is predicted. Likewise, the E_{OC} and corrosion rate may be predicted from the intercept between j_{cat} and $j_{diss.}$ For Mn_{20}, this occurs at $1x10^{-4}$ A (0.52 nmol s^{-1} cm^{-2} for n=2) and -0.35 V_{sce} in relatively good agreement with the experimental values. The E_{OC} during spontaneous passivation of Mn_{10} and Mn_{20}, remained on the leading edge of the dissolution transient, just above the a1 potential. To highlight this point, the form of the dissolution transient for Mn_5 is superimposed on the potential axis of **Fig. 5**. For these alloys, the cathodic activity was insufficient to reach the critical dissolution rate necessary for passivation to occur.

Spontaneous passivation was observed for at% Mn ≤ 6.5%. This occurred as a single dissolution transient for Mn_0 consistent with the residence time distribution (RTD) of the flow cell. This suggests that, in the absence of Mn, the spontaneous passivation process was too rapid to be resolved with the experimental protocol used here. The potential increased immediately above the a1 potential and then continued to increase progressively throughout the remainder of the experiment. The $Mn_{1.5}$ alloy showed a similar behavior. The critical dissolution potential was lower than for Mn_0, but beyond the initial peak, a period of slow rate decline was observed.

The situation is more complex for the Mn_5 and $Mn_{6.5}$ alloys. Two distinct kinetic

Journal Pre-proof

periods were observed: (1) an early sharp dissolution peak similar to that observed for Mn_0 and $Mn_{1.5}$ alloys, and (2) a period of significantly slower rate decline. The E_{OC} variation in this period corresponded to the traversing of the a2 maximum in the dissolution transient and was characterized by an abrupt increase in the rate of the potential change.

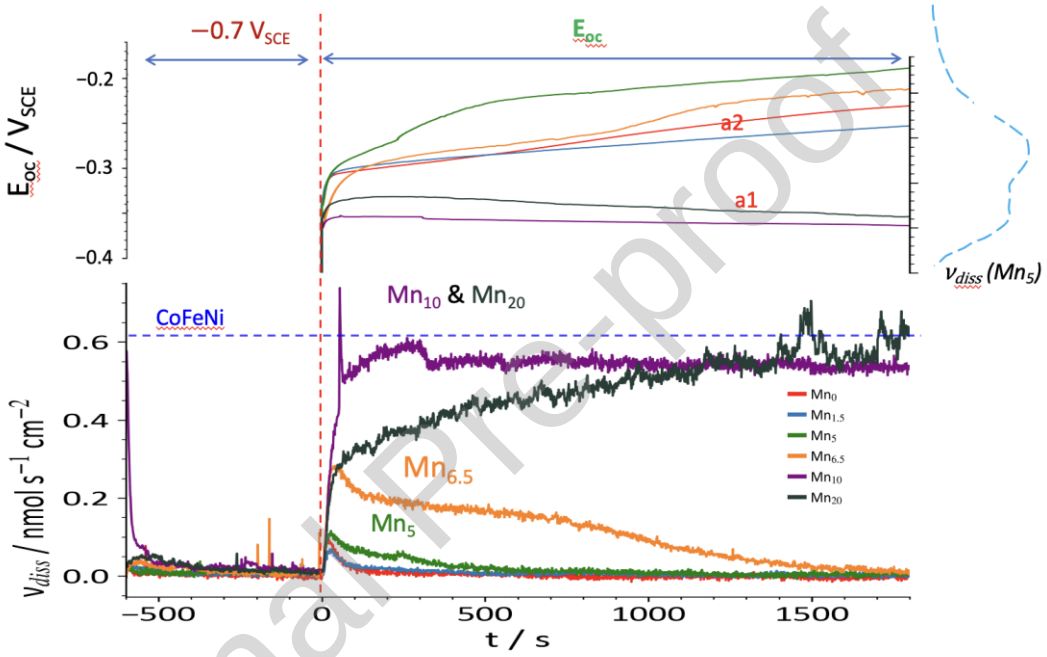

Fig. 5. The total dissolution rates of all $(CoCrFeNi)_{100-x}Mn_x$ alloys (at%) from cathodic activation at −0.7 V_{SCE} to E_{OC} over the first cycle of experiments, the other cycles may be found in supplementary materials (**Fig. S1**). Subplot (a) displays the potential curves at E_{OC}, a dissolution curve of Mn_5 alloy is plotted at the same potential axis to show the correlation between polarization and spontaneous passivation. While subplot (b) encompasses total dissolution of all tested alloys. The dashed blue line indicates the dissolution rate of CoFeNi alloy during the last 100 s of E_{OC} under the same experiment condition.

These results indicate a critical Mn concentration between 6.5 and 10 at%, above which spontaneous passivation will not occur in this electrolyte, at least on the time scale of these experiments. This correlates with the experimental Evans diagrams of **Fig. 3:** the extrapolated cathodic activity is greater than the critical dissolution rate at E_{pp} for at% Mn ≤ 6.5% predicting spontaneous passivation.

The method of sample preparation for the $(CoCrFeNi)_{(100-x)}Mn_x$ ($0 \leq x \leq 20$ at%) alloys implies that an increase in the concentration of Mn leads to a decrease in the

Journal Pre-proof

concentration of the other elements, and in particular, Cr: at% Cr = (100 – at% Mn)/4. It is therefore important to separate the effect of increasing at% Mn from that of decreasing at% Cr. This may be achieved by considering our previous work, [31], where the polarization curves and spontaneous passivation data for variable Cr in the absence of Mn were determined as a reference for this work.

The degree of spontaneous passivation may be estimated by the dissolution rate obtained at the end of the experiment, ν_{diss} (1750 s), determined as the average value between 1700 and 1800 s. **Fig. 6a** displays ν_{diss} (1750 s) as a function of at% Mn for Mn containing alloys and at% Cr for all alloys. The upper curve (in blue) shows the values obtained for the variable Mn alloys: $(CoCrFeNi)_{(100-x)}Mn_x$ while the lower curve shows the values obtained for $(CoFeNi)_{(100-x)}Cr_x$ (0% Cr) over the same concentration range. Note that for 0 at% Mn (25 at% Cr), ν_{diss} (1750 s) was below the $C_{3\sigma}$ detection limit and is not shown on the curve.

The efficiency of spontaneous passivation [31] has been defined as the quantity of alloy dissolved at the point where the dissolution rate has dropped to 30% of its maximum value, $Q_{diss}(30\%)$. **Fig. 6b** shows $Q_{diss}(30\%)$, as a function of at% Mn and at% Cr for both $(CoCrFeNi)_{(100-x)}Mn_x$ and $(CoFeNi)_{(100-x)}Cr_x$. It is observed that both measures reveal an abrupt increase between 6.5 and 10 at% Mn. By contrast, the variation with %Cr in the absence of Mn, was comparatively negligible. It is of particular interest to note that the final dissolution rate of the Mn_{10} and Mn_{20} were similar to that of the CoFeNi ternary alloy with 0 at% Cr and Mn (dashed horizontal line in **Fig. 5**). This result demonstrates that the negative effect of Mn addition at ≥ 10 at% completely negates the beneficial effect of Cr at 25%.

Journal Pre-proof

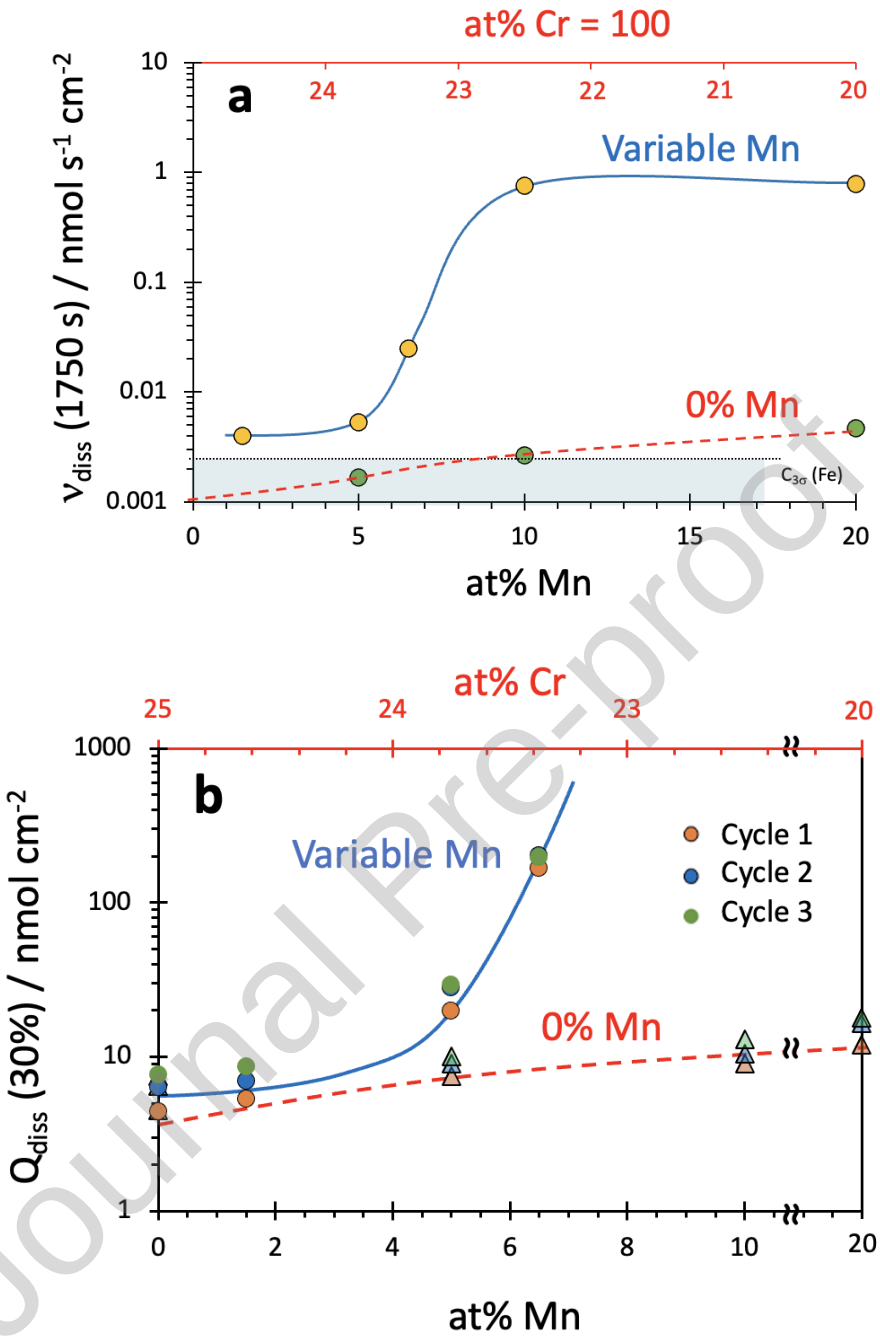

Fig. 6. Comparison of passivation metrics between variable Mn and variable Cr(a) (a) The dissolution rates during the last 100 s of the spontaneous passivation experiment (1700 – 1800 s). Results for the individual cycles are shown. (b) Cumulative dissolution quantities for each cycle during the first 300 s of the spontaneous passivation experiment, delineated against the Cr content in (and $(CoCrFeNi)_{100-x}Mn_x$ (blue) and $(CoFeNi)_{100-x}Cr_x$ (red) alloys. For the Mn_{10} and Mn_{20} alloys, the displayed quantities and rates correspond to values from a single cycle.

3.4 Elemental stoichiometry during spontaneous passivation

Journal Pre-proof

Fig. 7 displays the elemental dissolution curves of all passivated alloys during the first measurement cycle. The dissolution rate of Mn was normalized based on the nominal composition. The other cycles can be found in supplementary materials in **Fig. S2** and **S3**. During the activation period of all alloys, Cr showed the most notable dissolution while the dissolution of the other elements was negligible. In the early stages of dissolution, Mn_0, $Mn_{1.5}$ and Mn_5 alloys exhibit a significantly lower Cr dissolution rate than would be predicted from congruent dissolution, indicating the enrichment of Cr on the surface. The dissolution rate of Cr was slightly lower than that of the other elements during the first 40 s in $Mn_{6.5}$ alloy. Then, the dissolution rate of Cr rose above that of Co and Mn, which indicates the Cr enrichment is less pronounced during the initial stage and slows down after passive film formation.

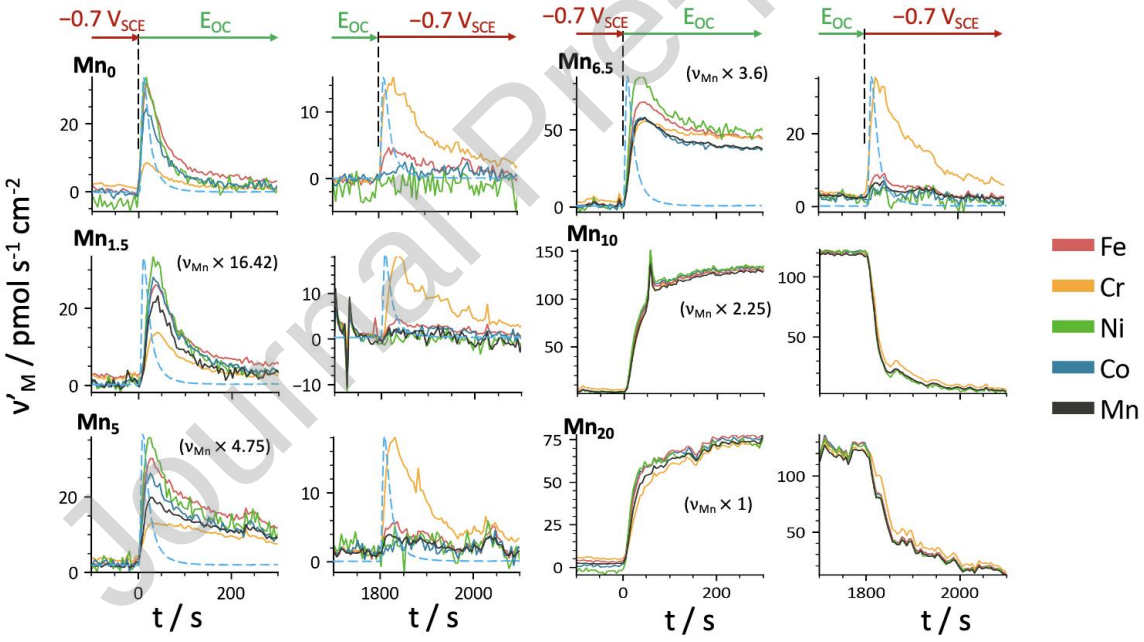

Fig. 7. Elemental dissolution profiles during (first and third columns) spontaneous passivation for the first 300 s; and subsequent activation from 1800 to 2100 s (second and forth columns). The dissolution rate of Mn was normalized based on the (nominal bulk composition) of $(CoCrFeNi)_{100-x}Mn_x$ alloys as indicated by the multiplier shown. The dashed curve gives the experimental residence time distribution of the flow cell. The other cycles are shown in supplementary materials (**Fig. S2 – S3**). A boxcar averaging (N = 5) was used for the AESEC results to improve the signal-to-noise ratio.

The enrichment of Cr during the early stages is more clearly indicated in **Fig. 8**. This shows the Cr and Fe dissolution rates on a log time scale to better resolve

Journal Pre-proof

graphically the two stages of spontaneous passivation. The Fe dissolution rate is shown as representative of the other elements but having the best signal to noise. Also shown is the estimated rate of Cr enrichment relative to Fe based on the difference in the (Fe – Cr) dissolution rates.

4.

$$\dot{\Theta} = d\Theta_{Cr/Fe}/dt = (\frac{X_{Cr}}{X_{Fe}})\nu_{Fe} - \nu_{Cr}$$

where X_{Cr} / X_{Fe} is the ratio of Cr to Fe in the bulk alloy.

It is clear from the results that the Cr enrichment occurred primarily during the first stage of passivation. This is particularly clear for $Mn_{6.5}$, where the two stages are best resolved, and dissolution was essentially congruent in the second stage.

The variation of the E_{OC} gives additional insight into the spontaneous passivation phenomenon: in every case where passivation occurs, the E_{OC} jumps to a value positive of the a1 peak immediately following the release of the cathodic activation potential. This immediate reaction gives rise to the rapid dissolution transient consistent with the form of the RTD and showing the most extensive degree of Cr enrichment.

In the second stage, the dissolution rate dropped off slowly while the potential continued to increase, ultimately rising above the a2 potential, with the Cr and Fe dissolution rates being essentially congruent. This would suggest that the second state reflects either a reorganization of the oxide film with enhanced barrier properties, or the continued growth of an oxide film but containing all the alloying elements making detection by AESEC impossible.

Journal Pre-proof

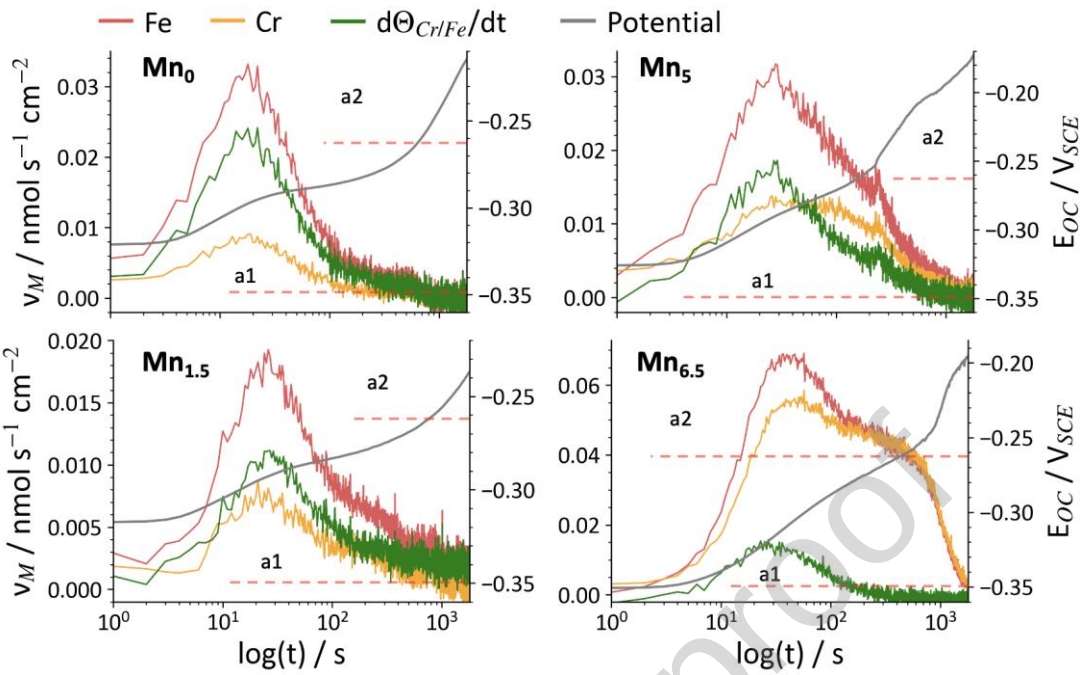

Fig. 8. The dissolution rates of Cr, Fe and the Cr enrichment relative to Fe during spontaneous passivation are plotted against a logarithmic time scale with E_{OC} values shown on a secondary y-axis. Only the first cycle is shown. The other cycles are shown in supplementary materials (**Fig. S4** and **S5**).

To better appreciate the relationship between spontaneous dissolution and the previously described polarization curves, **Fig. 9** shows the dissolution rate plotted as a function of the E_{OC}. For Mn_5 and $Mn_{6.5}$, the a1 and a2 peaks are detected, although the a2 reaction is broadened into a nearly linear rate vs. potential profile. The Mn_0 and $Mn_{1.5}$ peak were shifted in the positive direction from the a1 as observed in the polarization curves.

Journal Pre-proof

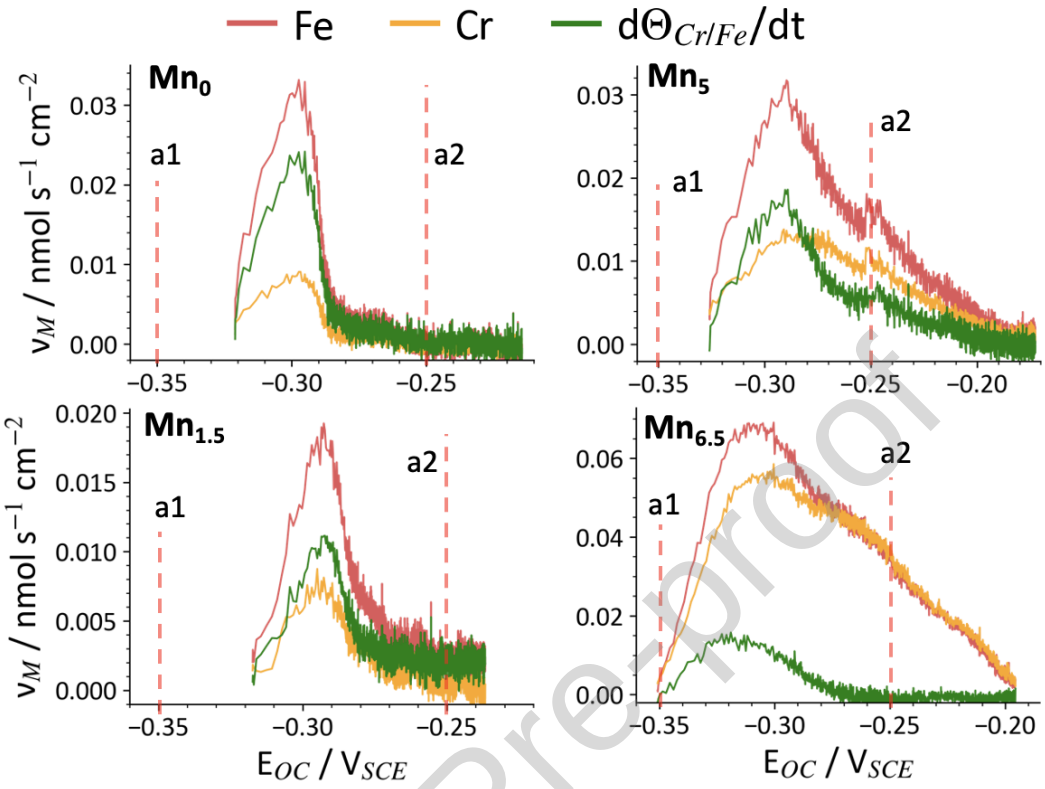

Fig. 9 The dissolution profiles as a function of E_{OC}. The dashed red vertical lines indicate the a1 and a2 potential as in **Fig. 4**. The other cycles for each alloy are shown in the Supplementary Materials (**Fig. S6** and **S7**).

4.0 Discussion

Mechanistic considerations

As pointed out by Michel Keddam in his review of anodic dissolution [34], a major interest of the polarization curve (j_e – E_{ap}) is to predict the behavior of a material over a wide range of potential. One difficulty of conventional electrochemistry is that the measured faradaic current is the sum of the anodic and cathodic currents. Element resolved electrochemistry allows us to determine directly the total alloy dissolution rate and the resulting j_{diss} – E_{ap} characteristic profile, combined with the j_e – E_{ap}, should be much more representative of the material than the latter by itself. For example, in the experimental Evans diagrams **(Fig. 3)** the active to passive transition is not detected in the j_e – E profile for the alloys of at% Mn ≤ 1.5 and the onset of anodic dissolution

Journal Pre-proof

was below $E_{j=0}$ for all alloys.

Further, two peaks were observed when the %Mn ≥ 5 at% suggesting different stages or mechanisms of dissolution. These peaks were not visible in the $j_e - E_{ap}$ profile. These two stages of passivation were also observed in the spontaneous j_{diss} - E_{OC} profile **(Fig. 9)** which may be thought of as analogous to the polarization curve only obtained at the free corrosion potential. The spontaneous dissolution results for Mn_5 and $Mn_{6.5}$ suggests that the first stages of passivation involve extensive Cr enrichment, followed by a period where dissolution is much more closely congruent. A likely explanation is that the first stage represents the formation of an initial Cr rich film followed by further oxidation of the alloy during which dissolution is blocked by the first film.

Previous research has demonstrated that the passive film formed in sulfuric acid was of a duplex nature, heavily enriched in Cr, with Mn(II) and other cations mainly present in the inner layer [10,35] with a Ni enriched metallic layer just below the passive film. The enrichment of Cr in the inner film would not be readily detected from the dissolution results since the all the elements would enter the oxide film. However, the continued formation of the film would be mirrored in the decrease of the spontaneous dissolution rate and increase of E_{OC}.

Comparison of **Fig. 9** with **Figs. 3** and **4** gives insight into the difference between forced passivation by the power supply of a potentiostat and spontaneous passivation, driven by the cathodic reaction on the surface. The addition of Mn to the alloy had little effect on the overall passive current in the passive domain, or transpassive potential in agreement with [11]. However, the dissolution rate in the final moments of spontaneous passivation **(Fig. 6a)** increased significantly with increasing at% Mn. Likewise, in the $j_{diss} - E_{ap}$ profile, the maximum dissolution rates ($j_{diss,crit}$) of Mn_5 and $Mn_{6.5}$ alloys were nearly identical during the active-passive transition, but during spontaneous passivation, the $Mn_{6.5}$ alloy showed an order of magnitude larger quantity of dissolution ($Q_{diss}(30\%)$) to achieve a 30% reduction in the rate **(Fig. 6)**. This difference arises because the applied potential forces a change in the electrochemical

Journal Pre-proof

process during polarization, accelerating the inherently slow active-passive transition, thus minimizing the difference. Without the applied potential, there is insufficient driving force, and the alloy remains near the critical dissolution rate for a longer time, resulting in much more dissolution.

This distinction is highlighted in **Fig. 10** which compares the $\nu_{Fe} - E_{OC}$ and $\nu_{Fe} - E_{ap}$ profiles for the $Mn_{6.5}$ alloy. This alloy was chosen because the time resolution of spontaneous passivation was sufficient to clearly distinguish the transient from that of the residence time distribution as shown in **Fig. 7**. As a reference the form of the log $|j_e|$ vs. E curve is also given, not to scale. For spontaneous passivation, the cathodic and anodic reaction occur on the same surface. Therefore, as the potential increases, the cathodic reaction decreases, and the final open circuit potential does not go far beyond the beginning of the passive domain in the $j_e - E_{ap}$ profile. By contrast, when passivation is driven by the power supply of the potentiostat with the cathodic reaction on a distant counter electrode, the potential will rise to any arbitrary value with a subsequent increase in the degree of oxidation and the thickness of the film, at least until the transpassive potential is obtained. In this case, all the alloys show passivation with similar passive and transpassive currents, independent of the %Mn, as shown in **Fig. 2.**

The schematic on the right of **Fig. 10** shows the most probable interpretation of the $\nu_{Fe} - E_{OC}$ based on this inner / outer passive film model for the $Mn_{6.5}$ alloy based on the model described above. The results of **Fig. 9** suggest that Cr enrichment occurs during the early stages of spontaneous passivation ($\nu_{Cr} < \nu_{Fe}$). After approximately 100 s, the dissolution became nearly congruent ($\nu_{Cr} \approx \nu_{Fe}$) although passivation continued to occur (decreasing ν_{Fe}). This result, and the steady increase in E_{OC}, are consistent with a continued oxidation of the alloy to form an oxide containing all the elements. In correlation with the previous structural investigations, this would correspond to the inner film. From the results of **Figs. 9** and **Fig. 11,** it would appear that this secondary oxide film is primarily responsible for lowering the dissolution rate. The formation of

Journal Pre-proof

the outer film lowers it by about 25%.

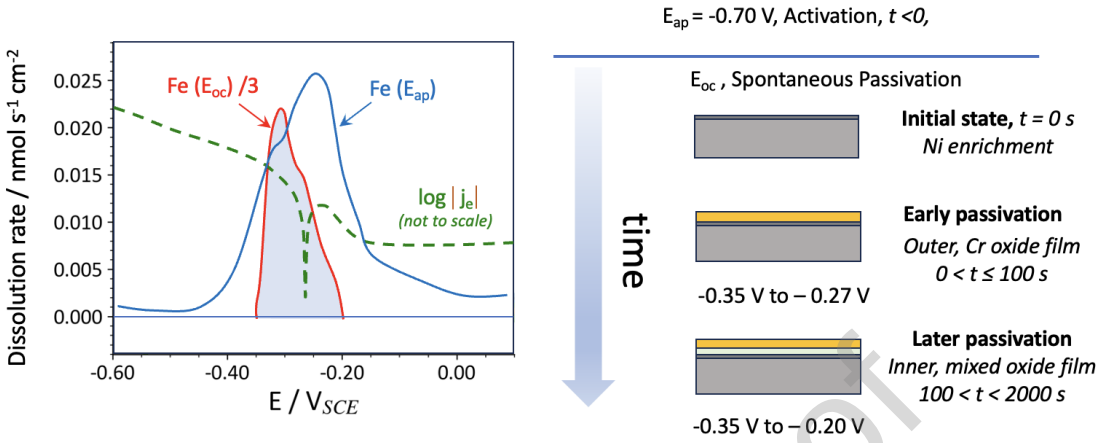

Fig. 10. Left: Overlay of the $\nu_{Fe} - E_{ap}$ (blue) and $\nu_{Fe} - E_{OC}$ (red) profiles and the form of the log $|j_{Fe}| - E_{ap}$ (blue) profiles. **Right:** A schematic model showing the stages of spontaneous passive film formation based on the previous surface characterizations.

As discussed in the introduction, Mn is a highly reactive element, and it is not surprising that its presence in the alloy will enhance its reactivity. In the absence of a uniform outer film, the continuous dissolution of metallic Mn into Mn^{2+}(aq) under spontaneous conditions, would shift the corrosion potential of the alloy in the cathodic direction below the passivation potential of Cr. Therefore, we would conclude that the formation of a uniform outer film is a first step in the passivation process and that Mn inhibits the formation of this film.

The difficulty of forming a uniform passive film in the presence of Mn may be rationalized from thermodynamic considerations. Mn-based oxides, *i.e.*, MnO, Mn_2O_3, and Mn_3O_4, have similar free energies of formation compared to other transition metal oxides [36] and therefore, a strong segregation of Cr and Mn in the presence of oxygen for the CoCrFeMnNi high entropy alloy has been predicted [37], which may explain the observed formation of inner Cr- and Mn-based passive films [10]. Due to their relatively high mixing Gibbs energy, Mn-based oxides are not favorable for mixing with other Cr-based oxides [33]. Thus, the detrimental effect of Mn-based oxide in the passive film may be driven by the phase separated oxides [33] preventing the Cr oxide

film from coalescing into a uniform passive film. The inner film with a stoichiometry more closely resembling the bulk alloy would only form once the outer film had formed and become sufficiently uniform to lower the alloy dissolution rate to a critical level.

The effect of variable Cr

The Mn_{10} and Mn_{20} alloys showed a similar dissolution rate as the Cr-free CoFeNi equiatomic alloy (approximately 0.58 nmol s^{-1} cm^{-2} [31]), indicating that the presence of Mn completely negates the presence of Cr in the Cantor alloy. The negating effect of Mn on Cr is illustrated in **Fig. 11** which shows the polarization and equivalent current curves on the left, with total dissolution curves on the right for Mn_5, Mn_{10}, and Mn_{20} alloys and their corresponding Mn-free alloys with equivalent Cr content. Polarization and AESEC equivalent current curves with identical Cr content show that Mn addition increases dissolution during the activate-passive transition, requiring more current and higher potential to complete the passivation process. As at% Mn increased, the active-passive transition potential shifted to higher values and ultimately split into two separate peaks.

The plots on the right-side of **Fig. 11** show that without Mn, the alloys passivate in less than 300 s in the at% Cr range of interest. As compared with Mn-free alloys of the same Cr content, the Mn_{10} and Mn_{20} alloys exhibited higher $E_{pp,diss}$ and $j_{crit,diss}$, indicating that a greater cathodic activity was necessary to drive the active-passive transition. The extrapolated cathodic activity on the polarization curves (**Fig. 11**, left) suggests that these two alloys cannot undergo spontaneous passivation, as confirmed by the dissolution profile (**Fig. 11**, right). Upon release of the activation potential, both alloys exhibit a rapid increase in dissolution rate and a continued dissolution, with the E_{OC} remaining at a low level, never exceeding the corresponding $E_{pp,diss}$. In contrast, the Mn-free alloy quickly undergoes spontaneous passivation, reaching a higher E_{OC} that surpasses $E_{pp,diss}$.

Journal Pre-proof

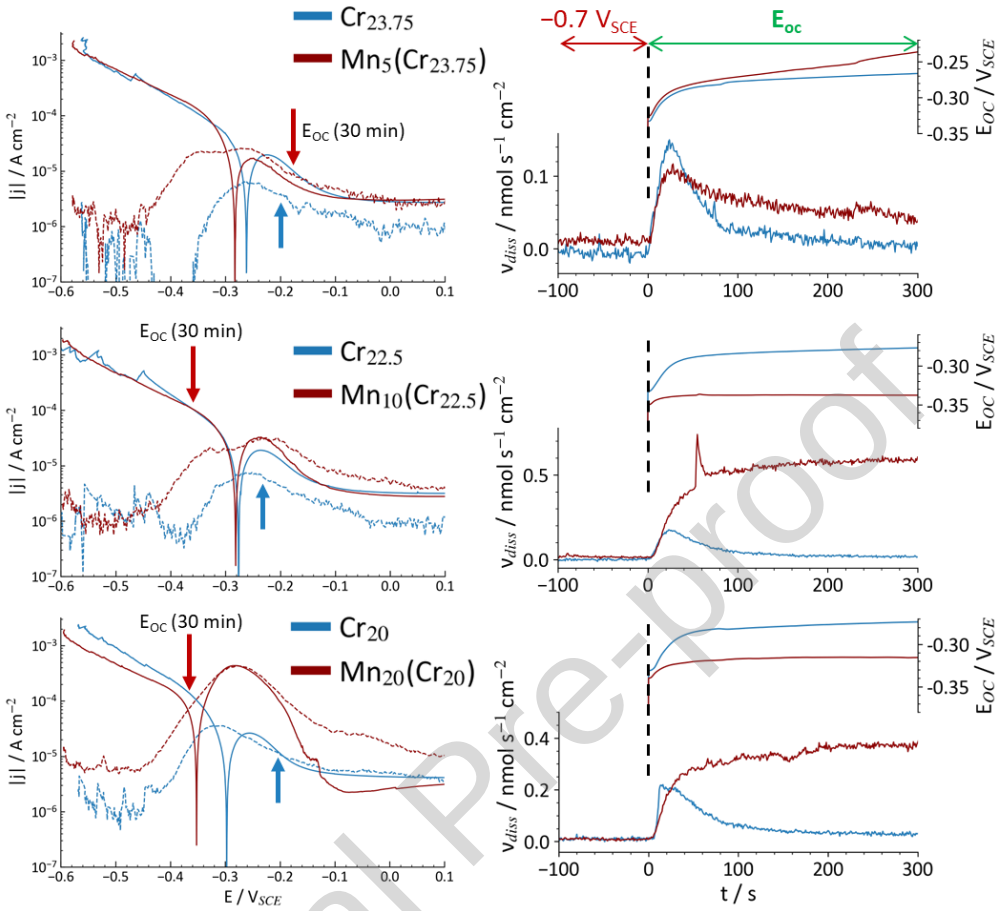

Fig. 11. Polarization and equivalent current curves are depicted on the left, with total dissolution curves (first 300 s) on the right, for Mn_5, Mn_{10}, and Mn_{20} alloys and their corresponding Mn-free alloys with equivalent Cr content. The Mn alloy curves are rendered in red, while the Mn-free alloy curves are in blue. Polarization measurements span a potential range from −0.7 to 0.1 V_{SCE}. The total dissolution curves encompass the transition from the last 100 s of activation to the initial 300 s of E_{OC} of the first cycle.

Journal Pre-proof

5. Conclusion

- Mn increases the reactivity of the Cantor family of alloys in aerated 0.1 M H_2SO_4, completely negating the effect of Cr at 10 at%. At 0 and 1.5 at% Mn, spontaneous passivation occurs rapidly on the order of the time resolution of the AESEC method. For 5 and 6.5 at% Mn, spontaneous passivation is significantly slower and involves the dissolution of a much larger quantity of

alloy. At 10 and 20 at% Mn, no spontaneous passivation was observed, and the open circuit dissolution (corrosion) rate was equivalent to CoFeNi ternary alloy.

- Spontaneous passivation could be predicted by examining the relationship between the position of the Tafel line extrapolated from the cathodic branch of the polarization curve, reaction and the dissolution current curve. When the cathodic current exceeds the critical dissolution rate during the active-passive transition, spontaneous passivation can occur. However, if the critical dissolution current is greater than the absolute cathodic current at the E_{pp}, spontaneous passivation will not occur, and the dissolution rate will not increase with the rise in transition current, as it is limited by the cathodic reaction rate.

- The onset of anodic dissolution begins below the $E_{j=0}$ potential. At < 1.5 at% Mn, a single active peak is observed that is completely below the $E_{j=0}$ and thus not detected in the conventional (j_e – E_{ap}) profile. At ≥ 5 at% Mn, the active to passive transition shows two poorly resolved peaks in the (j_{diss} – E_{OC}) profile, the higher potential peak increasing with increasing at% Mn. The addition of Mn shows limited influence on the cathodic reaction.

- The kinetics of spontaneous passivation is a dynamic process, where the cathodic reaction rate and anodic dissolution rate fluctuate with changes in surface potential differing significantly from passivation occurring at an applied potential.

CRediT author statement:

Chenyang Xie: Conceptualization, Data curation, Investigation, Methodology, Writing – original draft. **Junsoo Han:** Conceptualization, Writing – review and editing.

Journal Pre-proof

Fan Sun: Investigation, Resources, Writing – review and editing. **Kevin Ogle:** Conceptualization, Funding acquisition, Methodology, Supervision, Writing – review and editing.

Declaration of Competing Interest:

The authors declare that they have no known competing financial interests or personal relationships that could have appeared to influence the work reported in this paper.

Data Availability

Data will be made available on request.

Acknowledgements

This work was partially supported by the *Agence Nationale de Recherche*, France, grant #ANR-20-CE08-0031 (Tapas2020 project). We acknowledge the technical assistance of Junhui Tang.

References

[1] J.R. Scully, S.B. Inman, A.Y. Gerard, C.D. Taylor, W. Windl, D.K. Schreiber, P. Lu, J.E. Saal, G.S. Frankel, "Controlling the corrosion resistance of multi-principal element alloys", *Scr. Mater.* **188** (2020) 96–101. https://doi.org/10.1016/j.scriptamat.2020.06.065.

[2] J. Liu, Z. Lv, Z. Wu, J. Zhang, C. Zheng, C. Chen, D. Ju, L. Che, "Research progress on the influence of alloying elements on the corrosion resistance of high-entropy alloys", *J. Alloys Compd.* **1002** (2024) 175394. https://doi.org/10.1016/j.jallcom.2024.175394.

[3] B. Cantor, I.T.H. Chang, P. Knight, A.J.B. Vincent, "Microstructural development in equiatomic multicomponent alloys", *Mater. Sci. Eng. A* **375–377** (2004) 213–218. https://doi.org/10.1016/j.msea.2003.10.257.

[4] J.-W. Yeh, S.-K. Chen, S.-J. Lin, J.-Y. Gan, T.-S. Chin, T.-T. Shun, C.-H. Tsau, S.-Y. Chang, "Nanostructured high-entropy alloys with multiple principal elements: novel alloy design concepts and outcomes", *Adv. Eng. Mater.* **6** (2004) 299–303. https://doi.org/10.1002/adem.200300567.

Journal Pre-proof

[5] T. Aiso, M. Nishimoto, I. Muto, Y. Sugawara, "Roles of alloying elements in the corrosion resistance of equiatomic CoCrFeMnNi High-Entropy alloy and application to corrosion-resistant alloy design", *Mater. Trans.* **62** (2021) 1677–1680. https://doi.org/10.2320/matertrans.MT-M2021136.

[6] H.H. Uhlig, G.E. Woodside, "Anodic polarization of passive and non-passive chromium–iron alloys", *J. Phys. Chem.* **57** (1953) 280–283. https://doi.org/10.1021/j150504a005.

[7] I. Olefjord, "The passive state of stainless steels", *Mater. Sci. Eng.* **42** (1980) 161–171. https://doi.org/10.1016/0025-5416(80)90025-7.

[8] P. Marcus, J.M. Grimal, "The anodic dissolution and passivation of NiCrFe alloys studied by ESCA", *Corros. Sci.* **33** (1992) 805–814. https://doi.org/10.1016/0010-938X(92)90113-H.

[9] X. Li, P. Zhou, H. Feng, Z. Jiang, H. Li, K. Ogle, "Spontaneous passivation of the CoCrFeMnNi high entropy alloy in sulfuric acid solution: The effects of alloyed nitrogen and dissolved oxygen", *Corros. Sci.* **196** (2022) 110016. https://doi.org/10.1016/j.corsci.2021.110016.

[10] L. Wang, D. Mercier, S. Zanna, A. Seyeux, M. Laurent-Brocq, L. Perrière, I. Guillot, P. Marcus, "Study of the surface oxides and corrosion behaviour of an equiatomic CoCrFeMnNi high entropy alloy by XPS and ToF-SIMS", *Corros. Sci.* **167** (2020) 108507. https://doi.org/10.1016/j.corsci.2020.108507.

[11] J. Yang, J. Wu, C.Y. Zhang, S.D. Zhang, B.J. Yang, W. Emori, J.Q. Wang, "Effects of Mn on the electrochemical corrosion and passivation behavior of CoFeNiMnCr high-entropy alloy system in H_2SO_4 solution", *J. Alloys Compd.* **819** (2020) 152943. https://doi.org/10.1016/j.jallcom.2019.152943.

[12] D. Dworschak, K.-K. Tseng, J.-W. Yeh, H.-W. Cheng, M. Valtiner, "Bottom-up characterization of electrochemical passivity from simple binary alloys to high entropy alloys", *Electrochim. Acta,* **405** (2022) 139804. https://doi.org/10/gnzdxh.

[13] H. Luo, Z. Li, A.M. Mingers, D. Raabe, "Corrosion behavior of an equiatomic CoCrFeMnNi high-entropy alloy compared with 304 stainless steel in sulfuric acid solution", *Corros. Sci.* **134** (2018) 131–139. https://doi.org/10.1016/j.corsci.2018.02.031.

[14] A. Wetzel, M. von der Au, P.M. Dietrich, J. Radnik, O. Ozcan, J. Witt, "The comparison of the corrosion behavior of the CrCoNi medium entropy alloy and CrMnFeCoNi high entropy alloy", *Appl. Surf. Sci.* **601** (2022) 154171. https://doi.org/10.1016/j.apsusc.2022.154171.

Journal Pre-proof

[15] Q. Ye, K. Feng, Z. Li, F. Lu, R. Li, J. Huang, Y. Wu, "Microstructure and corrosion properties of CrMnFeCoNi high entropy alloy coating", *Appl. Surf. Sci.* **396** (2017) 1420–1426. https://doi.org/10.1016/j.apsusc.2016.11.176.

[16] J. Han, X. Li, A.Y. Gerard, P. Lu, J.E. Saal, G.S. Frankel, K. Ogle, J.R. Scully, "Potential dependent Mn oxidation and its role in passivation of $Ni_{38}Fe_{20}Cr_{22}Mn_{10}Co_{10}$ multi-principal element alloy using multi-element resolved atomic emission spectroelectrochemistry", *J. Electrochem. Soc.* **168** (2021) 051508. https://doi.org/10.1149/1945-7111/ac0062.

[17] H. Torbati-Sarraf, M. Shabani, P.D. Jablonski, G.J. Pataky, A. Poursaee, "The influence of incorporation of Mn on the pitting corrosion performance of CrFeCoNi high entropy alloy at different temperatures", *Mater. Des.* **184** (2019) 108170, https://doi.org/10.1016/j.matdes.2019.108170.

[18] S. Sahu, O.J. Swanson, T. Li, A.Y. Gerard, J.R. Scully, G.S. Frankel, "Localized corrosion behavior of non-equiatomic NiFeCrMnCo multi-principal element alloys", *Electrochim. Acta*, **354** (2020) 136749, https://doi.org/10.1016/j.electacta.2020.136749.

[19] S.B. Inman, J. Han, A.Y. Gerard, M.A. Wischhusen, S.R. Agnew, S.J. Poon, K. Ogle, J.R. Scully, "Effect of Mn content on the passivation and corrosion of $Al_{0.3}Cr_{0.5}Fe_2Mn_xMo_{0.15}Ni_{1.5}Ti_{0.3}$ compositionally complex face-centered cubic alloys", *Corrosion*, **78** (2022) 32-48, https://doi.org/10.5006/3906.

[20] Z. Szklarska-Smialowska, "Influence of sulfide inclusions on the pitting corrosion of steels", *Corrosion* **28** (1972) 388–396. https://doi.org/10.5006/0010-9312-32.8.309.

[21] Göran S. Eklund, "Initiation of pitting at sulfide inclusions in stainless steel", J*. Electrochem. Soc.*, **121**(1974)467-474. https://doi.org/10.1149/1.2401840.

[22] N. J. E. Dowling, C. Duret-Thual, G. Auclair, J.-P. Audouard, P. Combrade, "Effect of complex inclusions on pit initiation in 18% chromium-8% nickel stainless steel types 303, 304, and 321", *Corrosion* **51**(1995) 343–355. https://doi.org/10.5006/1.3293599.

[23] G. Wranglen, "Pitting and sulphide inclusions in steel", *Corros. Sci.* **14** (1974) 331–349. https://doi.org/10.1016/S0010-938X(74)80047-8.

[24] J. O. Park, T. Suter, H. Böhni, "Role of manganese sulfide inclusions on pit initiation of super austenitic stainless steels", *Corrosion*, **59** (2003) 59–67. https://doi.org/10.5006/1.3277537.

[25] Y.S. Lim, J.S. Kim, S.J. Ahn, H.S. Kwon, Y. Katada, "The influences of

Journal Pre-proof

microstructure and nitrogen alloying on pitting corrosion of type 316L and 20 wt.% Mn-substituted type 316L stainless steel", *Corros. Sci.*, **43** (2001) 53-68, https://doi.org/10.1016/S0010-938X(00)00074-3

[26] K. Park, H. Kwon, "Effects of Mn on the localized corrosion behavior of Fe-18Cr alloys", *Electrochim. Acta*, **55**(9) (2010) 3421-3427, https://doi.org/10.1016/j.electacta.2010.01.006

[27] M. Pourbaix "Atlas of Electrochemical Equilibria in Aqueous Solutions", Cebelcorr, 1966, second English edition, 1974.

[28] A. Erbe, M. Frederic Tesch, O. Rüdiger, B. Kaiser, S. DeBeer, M. Rabe, "Operando studies of Mn oxide based electrocatalysts for the oxygen evolution reaction", Phys. Chem. Chem. Phys. **25** (2023) 26958–26971. https://doi.org/10.1039/D3CP02384B.

[29] K.E. Heusler, On the passivity of manganese in acid solutions, J. *Electrochem. Soc.* **110** (1963) 703. https://doi.org/10.1149/1.2425853.

[30] C. Nyby, X. Guo, J. E. Saal, S.-C. Chien, A.Y. Gerard, H. Ke, T. Li, P. Lu, C. Oberdorfer, S. Sahu, S. Li, C. D. Taylor, W. Windl, J. R. Scully, G. S. Frankel, "Electrochemical metrics for corrosion resistant alloys", *Sci. Data* **8**, 58 (2021). https://doi.org/10.1038/s41597-021-00840-y.

[31] C. Xie, J. Han, J. Tang, F. Sun, K. Ogle, "The spontaneous passivation of $(CoFeNi)_{(1-x)/3}Cr_x$ alloys in sulfuric acid", *Corros. Sci.* **239** (2024) 112383. https://doi.org/10.1016/j.corsci.2024.112383.

[32] K. Ogle, "Atomic emission spectroelectrochemistry: Real-time rate measurements of dissolution, corrosion, and passivation", *Corrosion*, **75** (2019) 1398–1419, https://doi.org/10.5006/3336.

[33] K. Wang, J. Han, A.Y. Gerard, J.R. Scully, B.-C. Zhou, "Potential-pH diagrams considering complex oxide solution phases for understanding aqueous corrosion of multi-principal element alloys", *npj Mater. Degrad.*, **4** (2020) 4:35, https://doi.org/10.1038/s41529-020-00141-6.

[34] "Anodic Dissolution" in "Corrosion Mechanisms in Theory and Practice", 1st edition, J. Oudar and P. Marcus, *Marcel Dekker,* 1995.

[35] A. Y. Gerard, E. J. Kautz, D. K. Schreiber, J. Han, S. McDonnell, K. Ogle, P. Lu, J. E. Saal, G. S. Frankel, J. R. Scully, "The role of chromium content in aqueous passivation of a non-equiatomic $Ni_{38}Fe_{20}Cr_xMn_{21-0.5x}Co_{21-0.5x}$ multi-principal element alloy (x = 22, 14, 10, 6 at%) in acidic chloride solution", *Acta Mater.* **245** (2023) 118607. https://doi.org/10.1016/j.actamat.2022.118607

Journal Pre-proof

[36] L.-F. Huang, J.M. Rondinelli, “Reliable electrochemical phase diagrams of magnetic transition metals and related compounds from high-throughput ab initio calculations”, *npj Mater. Degrad.* **3** (2019) 1–13. https://doi.org/10.1038/s41529-019-0088-z.

[37] A. Ferrari, F. Körmann, “Surface segregation in Cr-Mn-Fe-Co-Ni high entropy alloys”, *Appl. Surf. Sci.* **533** (2020) 147471. https://doi.org/10.1016/j.apsusc.2020.147471.

CRediT author statement:

Chenyang Xie: Conceptualization, Data curation, Investigation, Methodology, Writing – original draft. **Junsoo Han:** Conceptualization, Writing – review and editing. **Fan Sun:** Investigation, Resources, Writing – review and editing. **Kevin Ogle:** Conceptualization, Funding acquisition, Methodology, Supervision, Writing – review and editing.

Declaration of interests

☒ The authors declare that they have no known competing financial interests or personal relationships that could have appeared to influence the work reported in this paper.

☐ The authors declare the following financial interests/personal relationships which may be considered as potential competing interests:

Journal Pre-proof

Highlights

Direct in situ measurement of the spontaneous passivation of CoCrFeNiMn alloy with variable Mn (0 – 20 at%).

Spontaneous passivation kinetics decreased with increasing Mn such that no passivation occurred above 10 at% Mn and the effect of Cr was negated.

Experimental Evans diagram approach was used to interpret spontaneous passivation kinetics. (Conventional polarization curve decoupled into anodic dissolution and cathodic reaction.)

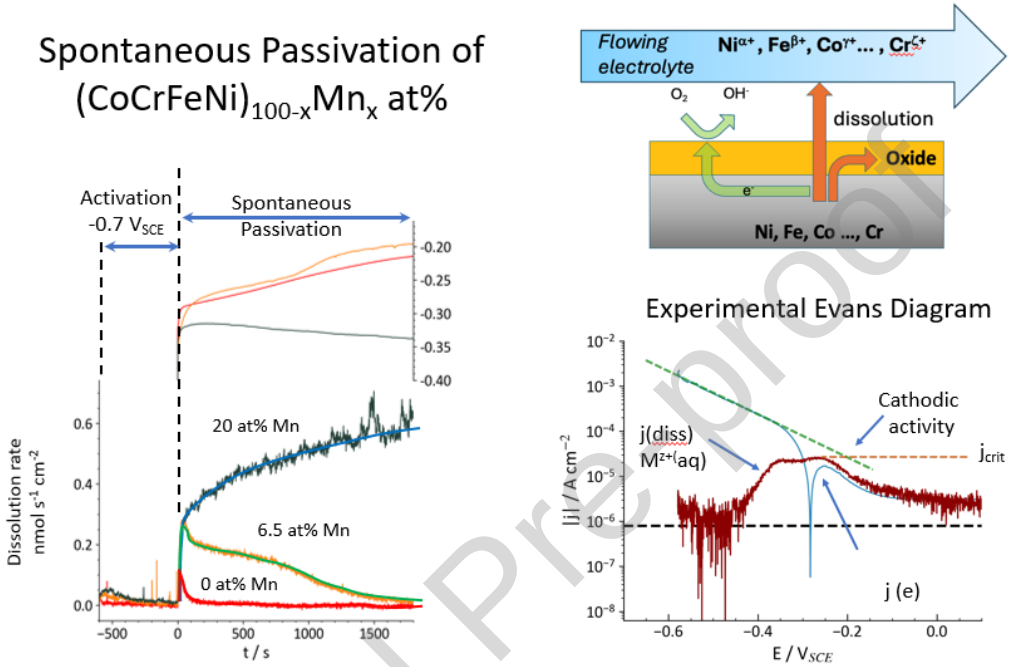

Journal Pre-proof